Research Square

Preprints are preliminary reports that have not undergone peer review.
They should not be considered conclusive, used to inform clinical practice,
or referenced by the media as validated information.

Tribocorrosion Behaviour of Sustainable Seashell-Derived Silicon Reinforced AZ91 Magnesium Composites: Interplay between Wear, Electrochemical Degradation and Interface Stability

Nikhil Gupta

nikhilofficial8510@gmail.com

Amity School of Engineering and Technology, Greater Noida Campus

Subodh Barthwal

Amity School of Engineering and Technology, Greater Noida Campus

Praveen Pachauri

Government Polytechnic Siwan

Research Article

Keywords: AZ91 magnesium composite, Tribocorrosion, Seashell-derived silicon, Wear and corrosion synergism, Interface stability, Sustainable reinforcement

Posted Date: November 6th, 2026

DOI: https://doi.org/10.21203/rs.3.rs-11043161/v1

License: This work is licensed under a Creative Commons Attribution 4.0 International License.
Read Full License

Additional Declarations: No competing interests reported.

Tribocorrosion Behaviour of Sustainable Seashell-Derived Silicon Reinforced AZ91 Magnesium Composites: Interplay between Wear, Electrochemical Degradation and Interface Stability

Nikhil Gupta[1*], Subodh Barthwal[2], Praveen Pachauri[3]
[1]Research Scholar, Mechanical Engineering, Amity School of Engineering and Technology, Greater Noida Campus, Uttar Pradesh, India.

[2]Associate Professor, Mechanical Engineering, Amity School of Engineering and Technology, Greater Noida Campus, Uttar Pradesh, India.
[3]Professor, Government Polytechnic Siwan, Bihar, India.

*Corresponding author- Nikhil Gupta (nikhilofficial8510@gmail.com)

Abstract

AZ91 magnesium alloys are interesting for their lightweight structural and biomedical applications, but their service life is reduced when mechanical sliding and chloride corrosion are combined. This kind of attack (tribocorrosion) erodes much more than wear or corrosion alone. The AZ91 was reinforced with Si particles recovered from waste seashells, and the influence of Si on wear, electrochemical corrosion, and interfacial stability of the Si-particle matrix was investigated in this work. Shell waste was subjected to calcination and reduction to obtain seashell-derived silicon (SDSi) particles, which were then added to the melt at 3, 6 and 9 wt% by stir casting. The microstructure, phase content, density, microhardness, static electrochemical testing, dry-sliding wear testing, and combined tribocorrosion testing were performed in 3.5 wt% NaCl. The composite with 6 wt% gave the best overall response. The microhardness value was approximately 102 HV, the corrosion current density decreased from ~95 to 34 μA cm−2, and the dry sliding wear rate decreased by almost 58% compared with the base alloy. The open-circuit potential of the 6 wt% composite was more stable under sliding conditions during tribocorrosion, and the synergy between wear and corrosion was reduced by over 50% compared to AZ91. The advantages were reversed at concentrations above 6 wt%, due to the formation of new galvanic sites and weak interfaces in particle clusters. The surfaces of the wear and tribocorrosion parts were analysed, and it was found that the composite exhibited a transition from deep AZ91 delamination and pitting to shallow abrasion and a more protective tribolayer. The findings reveal that if the reinforcement remains well dispersed and well bonded, a low-cost reinforcement derived from waste can enhance the durability of AZ91 under aggressive sliding contact.

Keywords: AZ91 magnesium composite; Tribocorrosion; Seashell-derived silicon; Wear and corrosion synergism; Interface stability; Sustainable reinforcement

1. Introduction

Magnesium and its alloys are the lightest structural metals in common engineering use, and this single property drives most of their appeal in transport, portable electronics and biodegradable implants [1, 2]. AZ91, with roughly 9 wt% aluminium and 1 wt% zinc, is the most widely cast member of the family because it combines good castability with reasonable strength [3]. The same chemistry that makes AZ91 easy to cast also leaves it vulnerable. Its microstructure contains a primary α-Mg matrix and a network of β-$Mg_{17}Al_{12}$ intermetallic, and the electrochemical mismatch between these two constituents sets up micro-galvanic cells as soon as a chloride film forms on the surface [4, 5]. The result is rapid dissolution of the matrix, hydrogen evolution and localised pitting [6, 7].

Limited hardness is another constraint for Magnesium when wearing occurs without any other impacts. This situation gets worse when there is both sliding and corrosion. In such cases, the thin corrosion product film is continuously removed by the moving contact, thereby reexposing the bare metal to the electrolyte repeatedly, and the overall thinning exceeds the sum of the two processes [8, 9]. This coupled loss is termed “tribocorrosion”, and the additional term is termed “wear-corrosion synergism” [10, 11]. The synergism can be so significant that it overwhelms the entire corrosion budget for a reactive metal like an Mg alloy, which is why many implant screws, pump components, and marine fittings made of Mg alloys are found to fail sooner than static corrosion data would suggest [12, 13].

A common approach to increasing the hardness and corrosion resistance of AZ91 is to incorporate a hard second phase. SiC, Si3N4, TiC, Al2O3, etc., ceramic particles will refine the grain structure, carry part of the applied load and blunt the wear scars [14, 15]. The tribocorrosion response of AZ91D has been enhanced by using metal oxide nanoparticles, and the results indicated that the thickness of the oxide tribolayer affects the friction coefficient and reduces the open circuit potential during sliding [16, 17]. These benefits are achievable, but the particles are typically purchased at high purity as powder, increasing costs and the environmental footprint of magnesium, which is already difficult to reconcile with the story of lightweighting [18].

The push to recover reinforcements from waste has led researchers to this dilemma. Fly ash, rice husk ash, and marine shell waste have been added to magnesium and aluminium matrices, sometimes for mechanical and corrosion benefits, similar to those of synthetic ceramics, at much lower cost [19, 20]. Sea shell waste is a significant stream of waste from the aquaculture industry, with a high calcium carbonate content and, with proper processing, a potential source of calcium- and silicon-rich ceramics [22, 23, 24]. A few studies have already demonstrated the reinforcement effect of seashell powder on the AZ31 magnesium alloy and its mechanical and biodegradation properties [25]. The missing piece is what happens with wear and corrosion, and whether the particle-matrix interface can withstand both.

In this research, waste seashells were processed into silicon-rich particles and then added to AZ91 via the stir-casting method at three different loadings. The degradation of AZ91 was divided into static corrosion, dry sliding wear and full tribocorrosion in 3.5 wt% NaCl. We decompose the total loss into mechanical, chemical, and synergistic terms, show how the reinforcement varies across each term, and then examine the worn and tribocorroded surfaces and relate them to interface stability.

2. Materials and Methods

2.1 Extraction and processing of seashell-derived silicon

Waste seashells were collected from a local coastal source, washed in distilled water to remove salt and organic residue, and dried at 110 °C for 12 h. The dried shells were crushed and ball-milled, then calcined at 900 °C for 3 h to drive off carbonate and organic matter and convert the biogenic calcium carbonate into a reactive calcium oxide precursor [22,24]. To obtain a silicon-bearing phase, the calcined powder was mixed with a silica source, reduced via a magnesiothermic route, and then acid-leached and washed to remove residual oxides and salts. The recovered powder is referred to here as seashell-derived silicon (SDSi). The powder was sieved to a mean particle size below 20 μm before use. Fig. 1. Gives the Schematic description of the sustainable synthesis of seashell-derived silicon (SDSi) reinforcement and its incorporation into AZ91 magnesium alloy through stir casting [21].

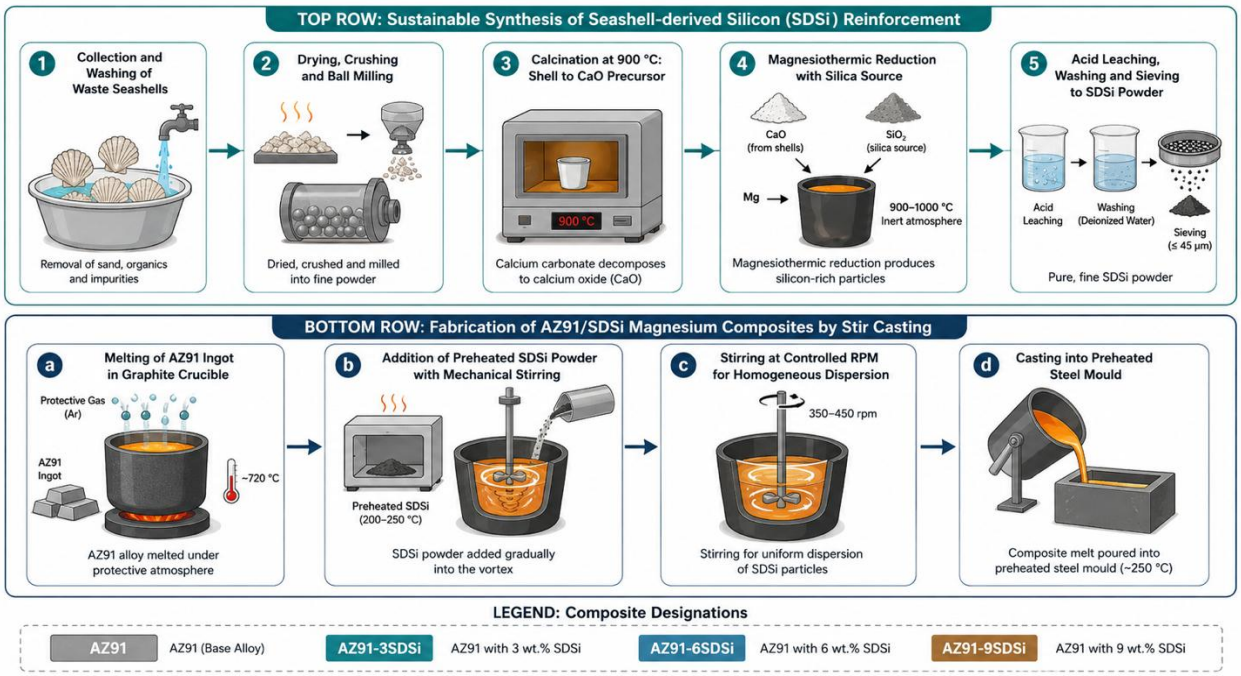


Fig. 1. Schematic of the seashell-derived silicon extraction route and stir casting of the AZ91/SDSi composites.

2.2 Fabrication of the composites

Commercial AZ91 ingots were used as the matrix; the nominal composition is given in Table 1. Composites were prepared by stir casting, a route chosen for its low cost and its ability to handle particle loadings in the range studied here [19, 26, 27]. The alloy was melted in a graphite crucible at about 720 °C under a protective cover gas to suppress oxidation and ignition. SDSi powder, preheated to around 300 °C to improve wetting and drive off moisture, was added to the melt while a coated steel impeller stirred at a controlled speed to create a vortex and pull the particles into the liquid [28]. After stirring, the melt was poured into a preheated steel mould. Three composites were produced at 3, 6 and 9 wt% SDSi, together with an unreinforced AZ91 reference. The designations and target compositions are listed in Table 2.

Table 1. Nominal chemical composition of the AZ91 matrix alloy (wt%).

Element	Al	Zn	Mn	Si	Fe	Cu	Mg
AZ91	8.9	0.7	0.22	0.05	0.004	0.02	Bal.

Values are representative and should be replaced with your supplier certificate or measured composition.

Table 2. Designation and composition of the fabricated materials.

Designation	AZ91 (wt%)	SDSi (wt%)
AZ91	100	0
AZ91-3SDSi	97	3

AZ91-6SDSi	94	6
AZ91-9SDSi	91	9

2.3 Microstructure and phase analysis

Samples were ground through successive SiC papers, polished to a mirror finish, and etched with a picric acid solution to reveal grain boundaries and the β-phase network. Microstructure was examined by optical microscopy and scanning electron microscopy (SEM) equipped with energy-dispersive X-ray spectroscopy (EDS) for elemental mapping. Phase content of the SDSi powder and the composites was checked by X-ray diffraction (XRD) with Cu Kα radiation over a 2θ range of 20 to 80 degrees. Grain size was estimated by the linear intercept method, and particle distribution was assessed from several SEM fields.

2.4 Density and hardness

Bulk density was measured using the Archimedes method and compared with the rule-of-mixtures value to estimate porosity. Vickers microhardness was recorded at a 100 g load, and a 15 s dwell, averaging at least eight indents per sample taken away from visible particle clusters.

2.5 Static electrochemical tests

Corrosion behaviour without sliding was measured in 3.5 wt% NaCl at room temperature using a three-electrode cell, with the sample as the working electrode, a saturated calomel reference and a platinum counter electrode. The exposed area was 1 cm^2. Samples were held at open circuit for 30 min to reach a steady potential, after which electrochemical impedance spectroscopy (EIS) was performed from 100 kHz to 10 mHz at the open-circuit potential with a 10 mV amplitude. Potentiodynamic polarization was followed, scanning from about −250 mV below to 250 mV above the open-circuit potential at 1 mV s^{-1}. Corrosion current density and potential were obtained by Tafel extrapolation, and EIS spectra were fitted to an equivalent circuit.

2.6 Dry sliding wear tests

Dry sliding wear was measured on a pin-on-disc tribometer against a hardened steel counterface. Tests were run at a normal load of 5 N, a sliding speed of 1 m $s^{-1,}$ and a sliding distance of 1000 m at room humidity. The friction coefficient was logged continuously. Wear was quantified from mass loss and converted to a volumetric wear rate. Each condition was repeated three times.

2.7 Tribocorrosion tests

Tribocorrosion tests combined the pin-on-disc contact with the three-electrode cell so that sliding and electrochemistry were recorded together in 3.5 wt% NaCl [10, 16]. The open-circuit potential was tracked before, during, and after sliding at 5 N. The total mass loss under tribocorrosion was separated into a mechanical component measured under cathodic protection, a pure corrosion component measured without sliding, and a synergistic component obtained as the difference between the total loss and the sum of the first two [8, 11].

3. Results and Discussion

3.1 Characterization of the seashell-derived silicon reinforcement

XRD of the processed powder confirmed that the reduction route produced crystalline silicon, with residual calcium-bearing phases that survived leaching, as shown in Fig 2. SEM revealed angular to subrounded particles below 20 µm, and EDS confirmed that silicon was the dominant element, with minor amounts of calcium and oxygen, as shown in Fig. 3. The particle morphology matters for the composite because angular particles mechanically anchor in the matrix and resist pull-out during sliding, while residual calcium phases can influence the local electrochemistry once the particle is exposed [22, 24].

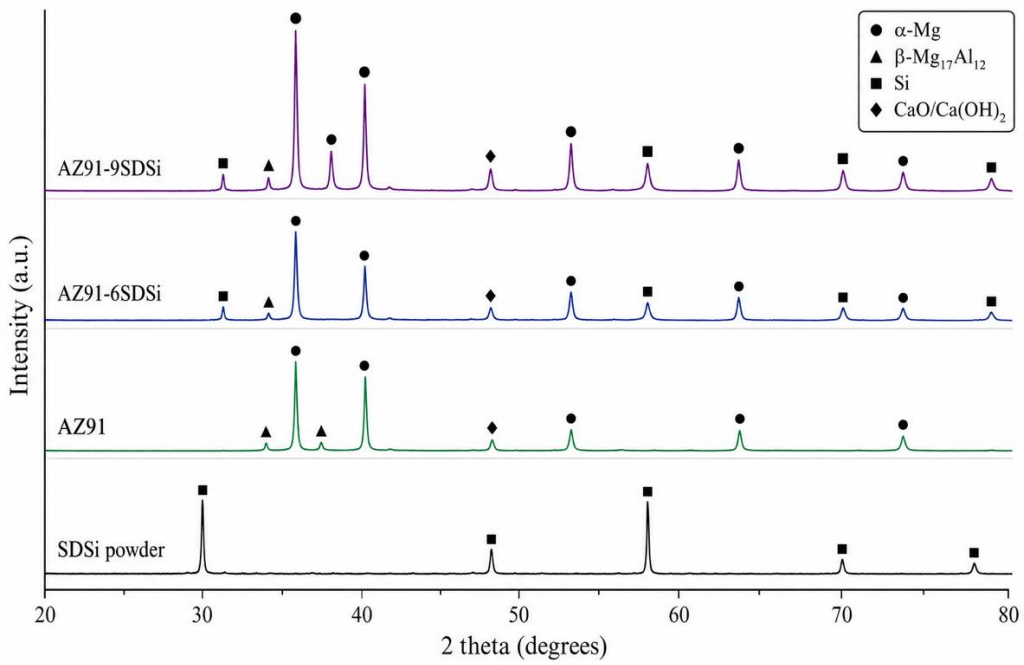


Fig. 2. XRD patterns of the seashell-derived silicon powder and the AZ91/SDSi composites showing the silicon reflections against the α-Mg and β-Mg17Al12 peaks

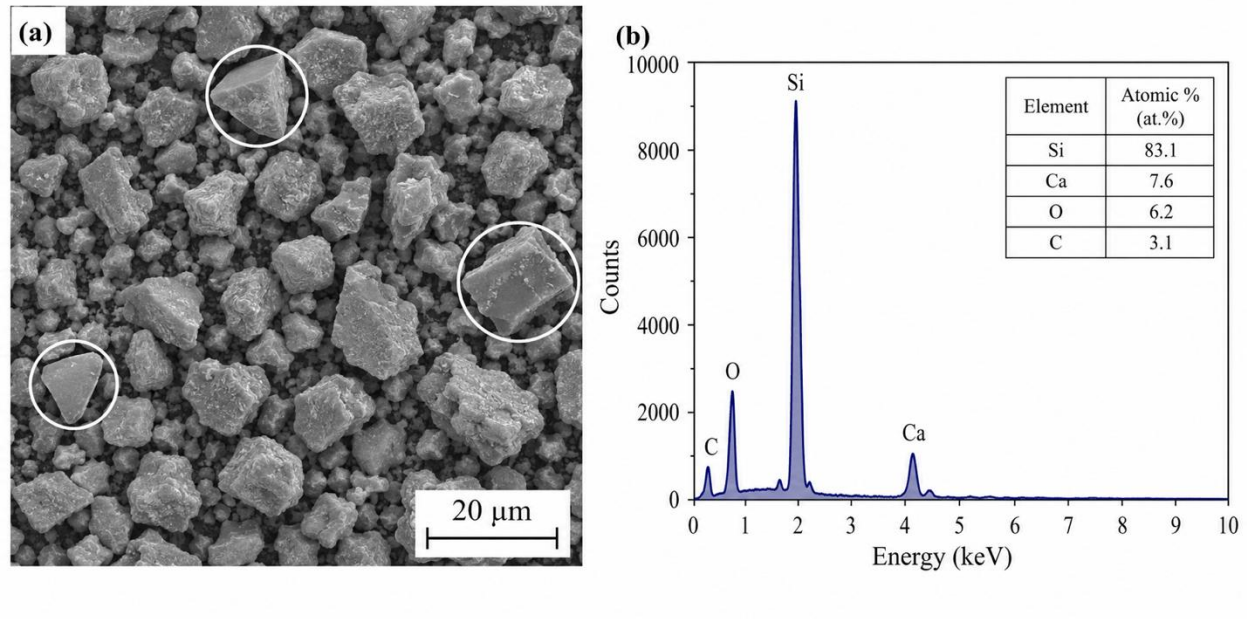


Fig. 3. SEM micrograph and EDS spectrum of the seashell-derived silicon particles.

3.2 Microstructure and phase distribution

The as-cast microstructure of the cast AZ91 reference exhibited the typical structure of this alloy, namely a coarse α-Mg matrix with a partially continuous β-Mg17Al12 network around the grain boundaries [4, 6, 7]. The addition of SDSi refined the grains as particles provide nucleation sites during solidification and hold the grain boundaries back from growth [26, 29]. The grain size decreased gradually up to 6 wt%, and the β phase was not continuous, but was fine and evenly distributed. This redistribution can be important for corrosion, as a fine, well-dispersed β network acts as a barrier to corrosion, whereas a coarse, sparse β phase acts as a good galvanic cathode, driving matrix dissolution [5]. The particles clustered at 9 wt%, causing porosity and interfering with the β distribution, which led to the subsequent reversal in the corrosion and wear results. Representative microstructures are shown in Fig. 4.

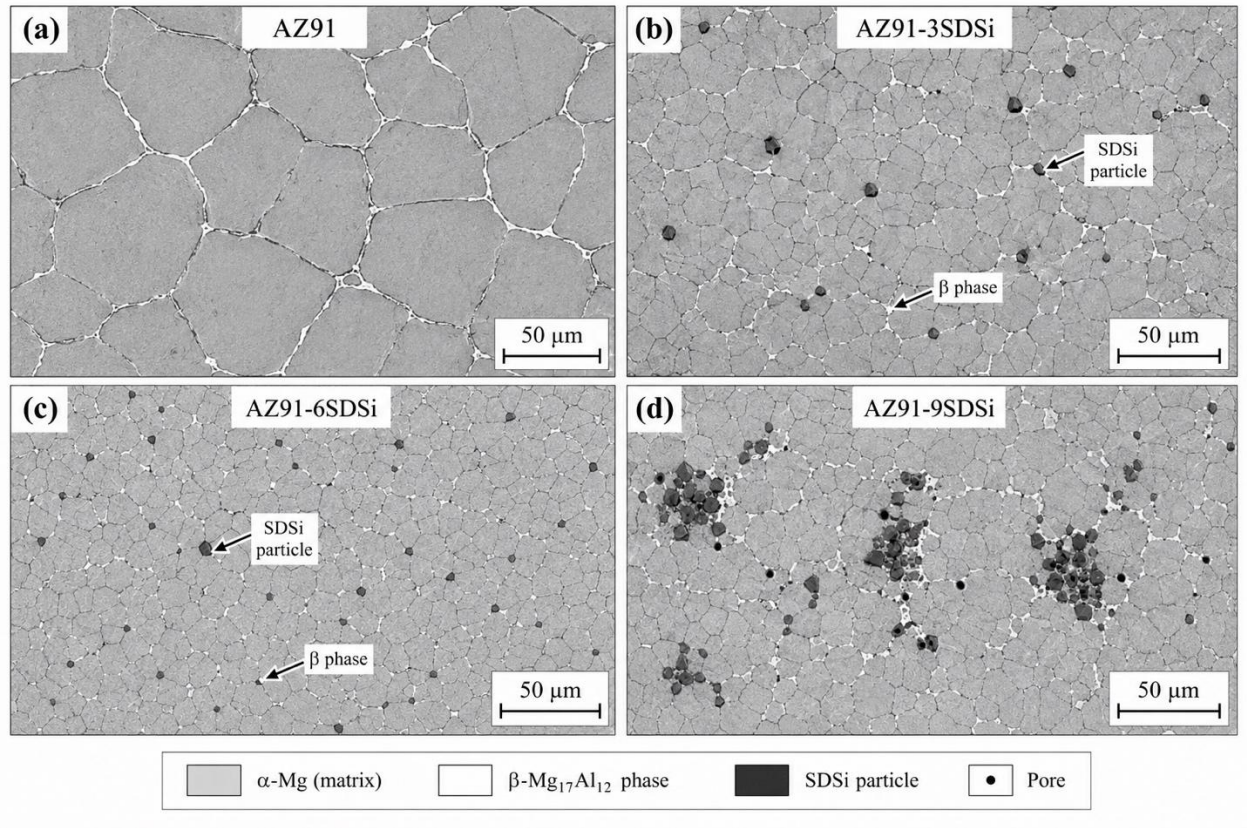


Fig. 4. Microstructures of (a) AZ91, (b) AZ91-3SDSi, (c) AZ91-6SDSi and (d) AZ91-9SDSi showing grain refinement, β phase redistribution and, at 9 wt%, particle clustering.

3.3 Density, porosity and hardness

Measured density remained close to the rule-of-mixtures value at low loadings, with porosity below about 2%. At 9 wt%, the porosity climbed as clusters trapped gas and hindered feeding during solidification, a known limit of stir casting at higher particle content [27, 28]. Microhardness rose with reinforcement, from about 68 HV for AZ91 to a peak near 102 HV at 6 wt%, an increase of roughly 50%. The gain comes from grain refinement through the Hall-Petch effect, from load transfer to the hard particles, and from the higher dislocation density generated by the thermal expansion mismatch between silicon and magnesium. Above 6 wt%, the hardness levelled off, then dropped slightly, as clustering and porosity offset the strengthening. The measured values are collected in Table 3 and Fig. 5.

Table 3. Density, porosity and Vickers microhardness of the fabricated materials.

Material	Density (g cm^{-3})	Porosity (%)	Microhardness (HV)
AZ91	1.81	0.9	68 ± 3
AZ91-3SDSi	1.83	1.4	84 ± 3

AZ91-6SDSi	1.85	1.8	102 ± 4
AZ91-9SDSi	1.84	3.1	96 ± 5

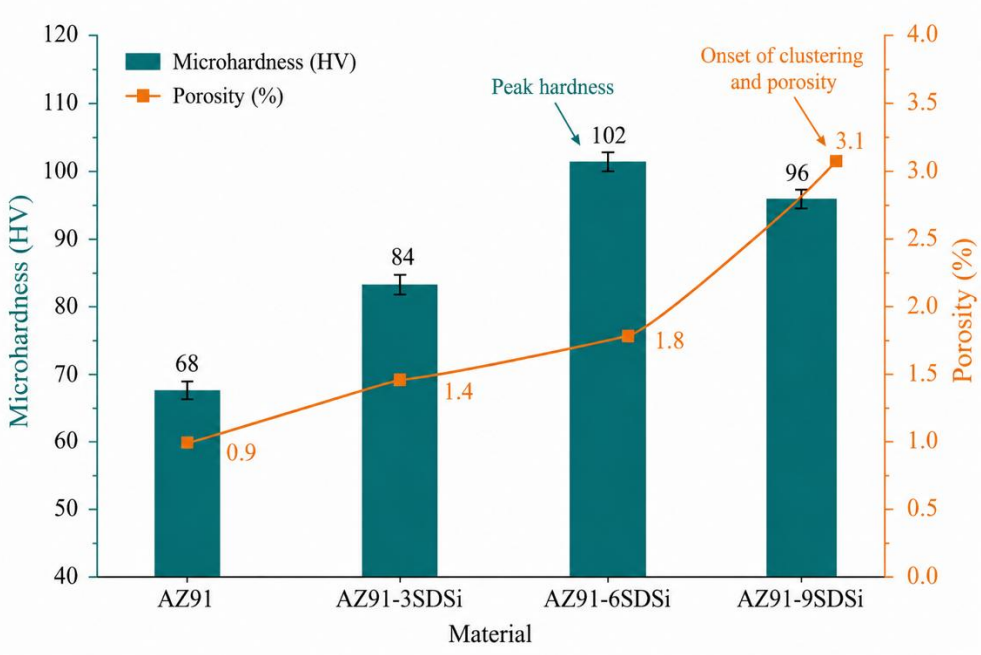


Fig. 5. Microhardness and porosity of AZ91 and the AZ91/SDSi composites as a function of reinforcement content.

3.4 Static electrochemical corrosion

The results of potentiodynamic polarization in 3.5 wt% NaCl solution demonstrate a clear improvement of reinforcement up to 6 wt%. The corrosion potential became more noble, and the corrosion current density for the AZ91 was about 95 μA cm^{-2}, whereas that for the AZ91-6SDSi was about 34 μA cm^{-2}, representing a reduction of approximately 60% in the corrosion rate. The better-distributed, finer grains of the β phase produce a more uniform surface, which can maintain a more uniform corrosion product film and minimize the size of any single micro-galvanic couple [34]. EIS confirmed the same. The 6 wt% composite had the highest charge-transfer resistance, increasing from approximately 480 Ω cm2 for AZ91 to approximately 1350 Ω cm^2, suggesting that the interfacial reaction rate is reduced and that the film is more protective [35]. Both measures deteriorated at 9 wt%. The clusters reveal silicon and residual calcium phases at a different potential than the matrix, thus creating new cathodic sites, while the porosity associated with the clusters allows the electrolyte to have easy access to the bulk [36]. The values of the parameters obtained by fitting are given in Tables 4 and 5, and the curves are illustrated in Figs. 6 and 7.

Table 4. Potentiodynamic polarization parameters in 3.5 wt% NaCl.

Material	E_corr (V vs SCE)	i_corr (µA cm⁻²)	βa (mV dec⁻¹)	βc (mV dec⁻¹)	Corr. rate (mm y⁻¹)
AZ91	−1.55	95	95	210	2.14
AZ91-3SDSi	−1.50	62	88	190	1.40
AZ91-6SDSi	−1.42	34	78	175	0.77
AZ91-9SDSi	−1.47	58	90	195	1.31

Table 5. Equivalent circuit parameters from EIS fitting in 3.5 wt% NaCl.

Material	R_s (Ω cm²)	R_ct (Ω cm²)	CPE (µF cm⁻²)	n
AZ91	11	480	18.5	0.86
AZ91-3SDSi	12	820	14.2	0.88
AZ91-6SDSi	12	1350	9.8	0.90
AZ91-9SDSi	11	760	15.1	0.87

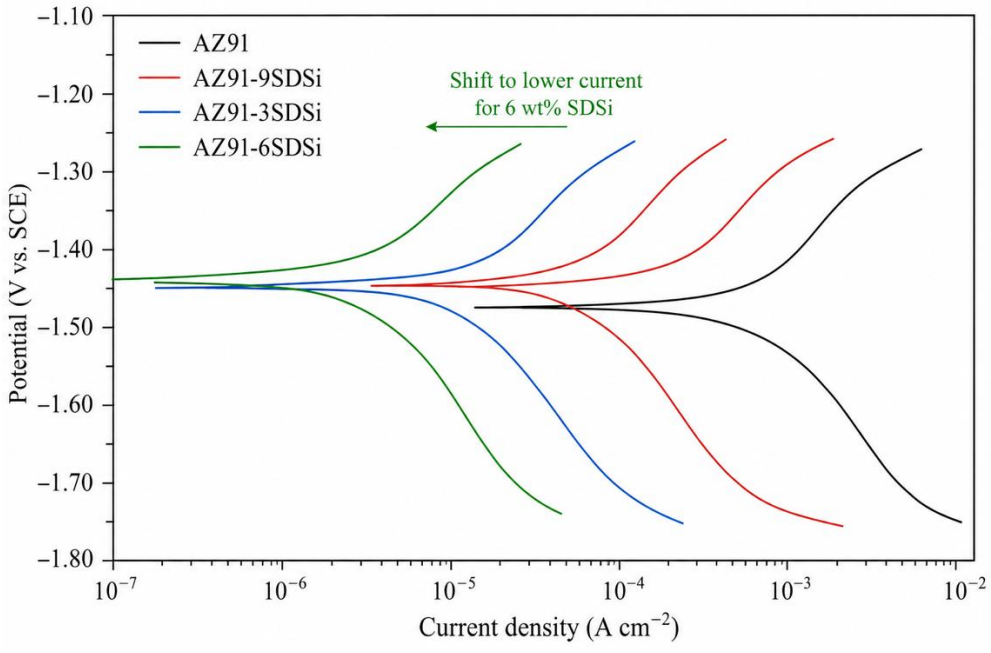


Fig. 6. Potentiodynamic polarization curves of AZ91 and the AZ91/SDSi composites in 3.5 wt% NaCl.

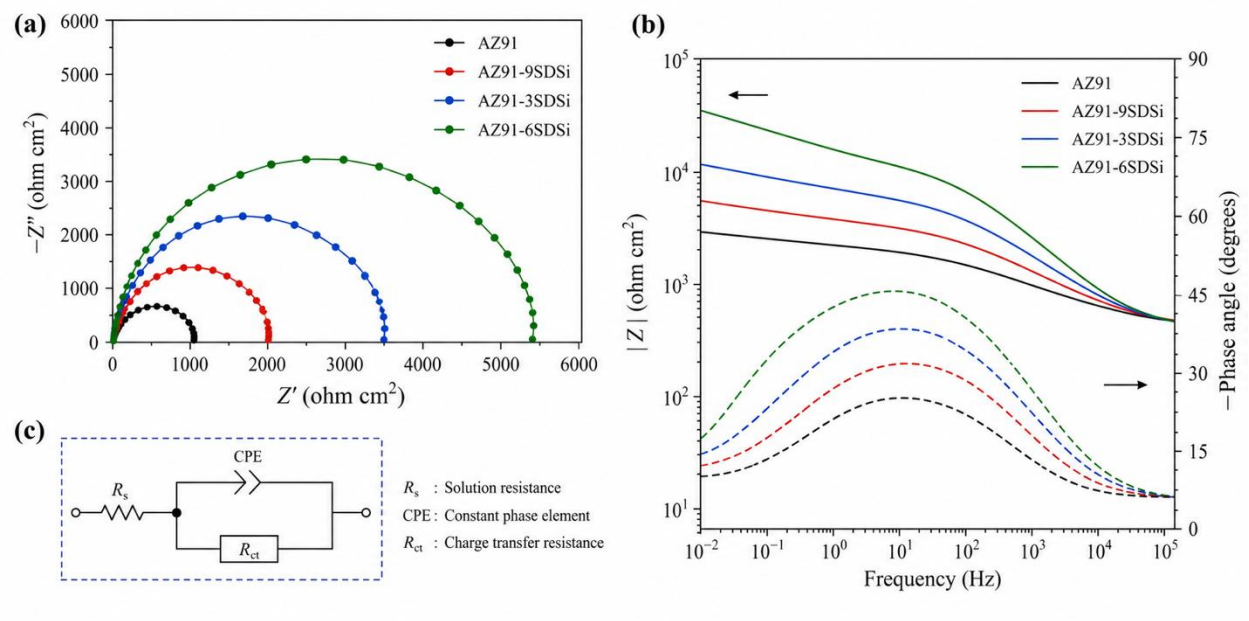


Fig. 7. Nyquist and Bode plots with the fitted equivalent circuit for AZ91 and the AZ91/SDSi composites in 3.5 wt% NaCl.

3.5 Dry sliding wear

Under dry sliding conditions, the reinforcement reduced both the friction coefficient and the wear rate. The friction coefficient of AZ91 averaged about 0.42 and fell to about 0.31 for the 6 wt% composite, while the volumetric wear rate dropped by close to 58% over the same range. Hard SDSi particles carry part of the contact stress, resist ploughing by the counterface and support a thin oxide and debris tribolayer that shields the softer matrix [15]. The dominant mechanism on AZ91 was delamination with clear signs of plastic smearing, whereas the 6 wt% composite showed mainly fine abrasion with a smoother track. At 9 wt%, the wear rate rose again because particles pulled out of the weaker clustered regions and then acted as third-body abrasive, scoring the surface they were meant to protect [38, 39]. The wear data are given in Table 6 and Fig. 8.

Table 6. Dry sliding wear results at 5 N, 1 m s^{-1} and 1000 m.

Material	Coeff. of friction	Wear rate (10^{-3} mm^3 m^{-1})	Specific wear rate (10^{-} mm^3 N^{-1} m^{-1})
AZ91	0.42	3.80	7.60
AZ91-3SDSi	0.36	2.55	5.10
AZ91-6SDSi	0.31	1.60	3.20
AZ91-9SDSi	0.34	2.20	4.40

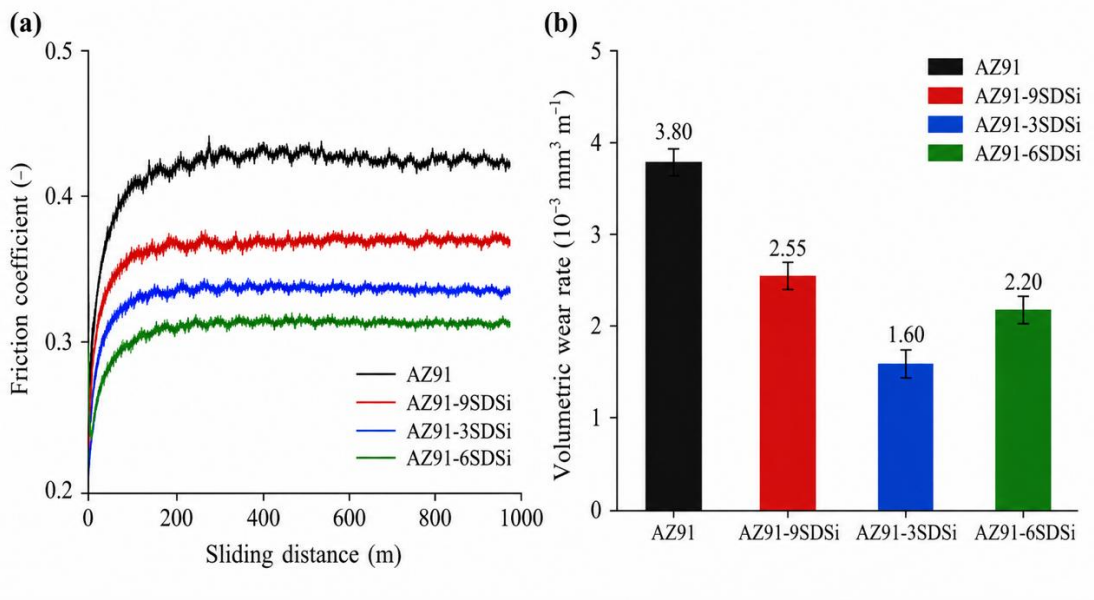


Fig. 8. Friction coefficient against sliding distance (a) and volumetric wear rate (b) for AZ91 and the AZ91/SDSi composites under dry sliding.

3.6 Tribocorrosion behaviour and wear and corrosion synergism

The tribocorrosion tests were the most effective in showing differences between the materials. The onset of sliding coincided with a dramatic drop in the open-circuit potential of each sample, characteristic of depassivation of the area under a moving contact [8, 10]. The magnitude of this drop and how rapidly the potential recovers following cessation of sliding provide useful criteria for assessing a surface's capability to self-repair. The potential drop was highest for AZ91, and the recovery was slow and noisy, indicative of ongoing film removal and repeated exposure of bare metal. The 6 wt% composite exhibited a more stable potential during sliding and rapid recovery upon re-separation of the sliding surfaces, suggesting the presence of a tougher, firmly established tribo-layer that was not easily removed by sliding [27].

For AZ91, the synergistic term was significant and accounted for a large portion of the total loss, indicating that the loss due to wear and corrosion was greater than the sum of its parts. Reinforcement reduced this synergism by over 50% at 6 wt%. Here, two effects are combined. The hard particles slow the mechanical removal of the film, resulting in fewer areas of bare metal exposed per pass, while the more protective film formed on the refined microstructure repassivates more quickly between passes, allowing the bare metal to exist for a shorter period before it dissolves. Recent research on magnesium has demonstrated that an appropriate dispersion of

second phases can form a self-reinforcing tribolayer that stabilizes the potential and protects the matrix, and the present results suggest that a well-dispersed SDSi reinforcement may do the same [30]. At 9 wt%, the synergism increased again due to particles being pulled out, which increased abrasion and created new galvanic and porosity pathways that removed the protection [38]. The partitioned losses are presented in Table 7, while the breakdown of the potential traces and synergism is shown in Fig. 9 and Fig. 10, respectively.

Table 7. Partition of tribocorrosion material loss in 3.5 wt% NaCl at 5 N.

Material	Total loss K_t	Mechanical K_w	Chemical K_c	Synergism S	S share (%)
AZ91	6.90	3.20	1.05	2.65	38
AZ91-3SDSi	4.55	2.30	0.70	1.55	34
AZ91-6SDSi	2.55	1.55	0.40	0.60	24
AZ91-9SDSi	3.85	2.05	0.65	1.15	30

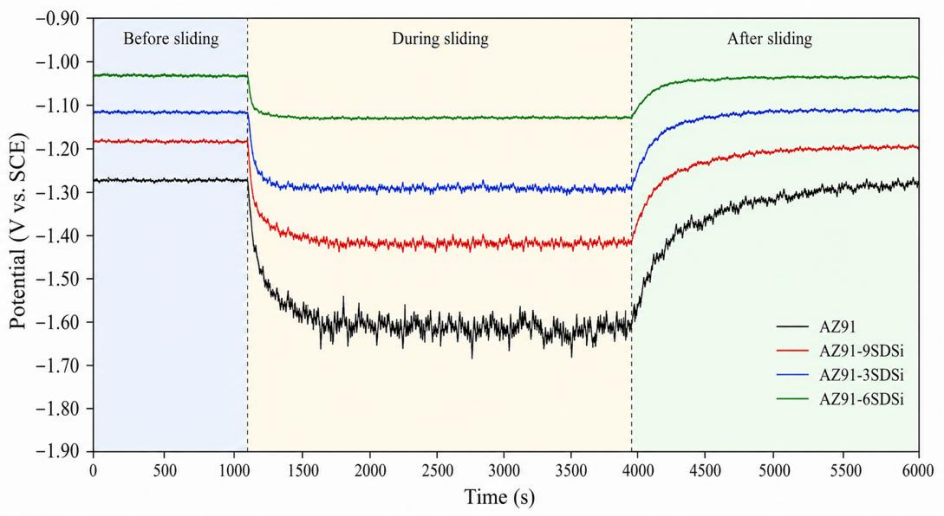


Fig. 9. Open circuit potential during tribocorrosion showing the potential drop when sliding starts and the recovery after sliding stops.

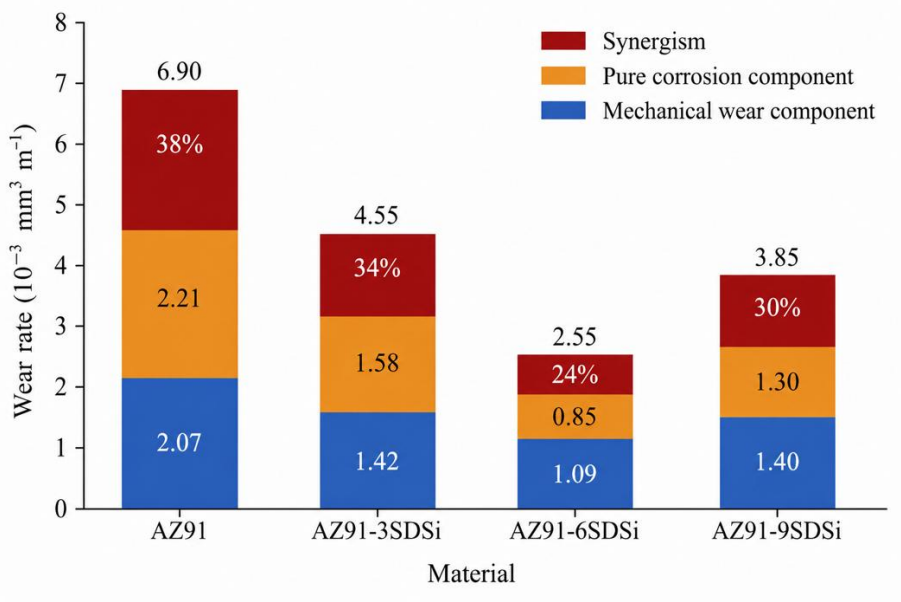


Fig. 10. Partition of tribocorrosion material loss into mechanical, chemical and synergistic components for AZ91 and the AZ91/SDSi composites.

3.7 Worn and tribocorroded surfaces

The surface analysis shown in Fig. 11 tied the numbers to physical mechanisms. Dry-worn AZ91 showed deep grooves, delaminated flakes and smeared material, the marks of adhesive and delamination wear on a soft matrix. The tribocorroded AZ91 surface exhibited numerous pits and cracked corrosion products in that picture, indicating that the protective film repeatedly broke under contact and was then attacked by the electrolyte [40]. The 6 wt% composite looked different. Its dry track was shallow, with fine abrasion marks, and its tribocorroded surface carried a more continuous, adherent tribolayer with only small, isolated pits. EDS across the track showed higher oxygen and silicon in the composite tribolayer, which supports the idea that SDSi particles and their oxides help build a mixed film that resists both removal and dissolution [42]. The 9 wt% surface showed pull-out cavities and third-body scoring, the visible cost of weak interfaces in the clustered regions [39].

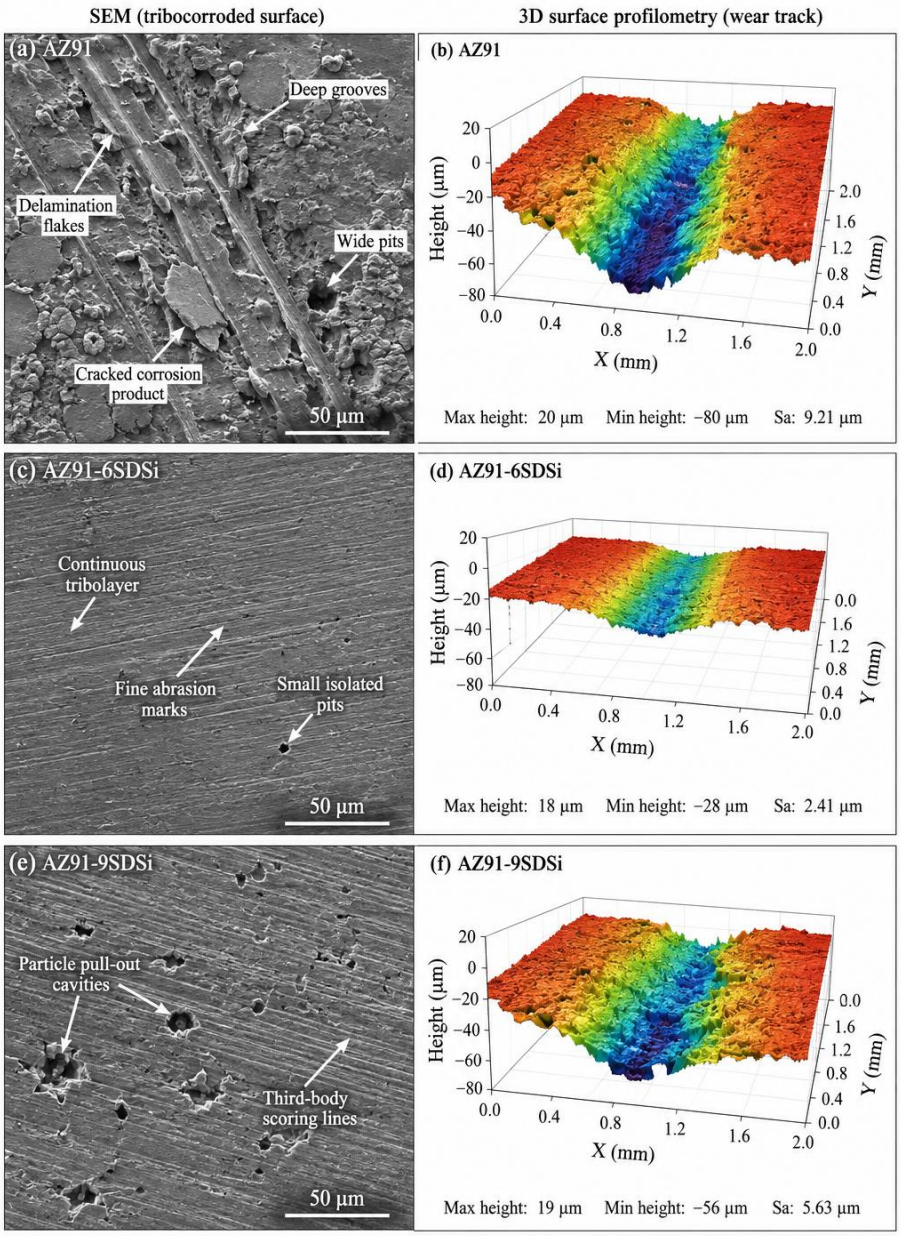


Fig. 11. SEM images of worn and tribocorroded surfaces with 3D wear-track profiles: (a, b) AZ91, (c, d) AZ91-6SDSi and (e, f) AZ91-9SDSi.

3.8 Interface stability and the design window

Reading the corrosion, wear and tribocorrosion results together, one variable controls the outcome, and that is the stability of the particle and matrix interface. Where SDSi particles are well dispersed and firmly bonded, as in the 3 and 6 wt% composites, they refine the grains, redistribute the β phase into a barrier configuration, carry load and anchor a durable tribolayer. In this state the

reinforcement improves every measure at once. Where the particles cluster, as at 9 wt%, the interfaces are weak, porosity rises, and the same particles become sites for pull-out, third-body abrasion and fresh galvanic attack. The reinforcement then works against the alloy [36, 38, 39]. The practical message is that there is a design window, near 6 wt% for the route used here, in which a waste-derived reinforcement gives real durability gains under combined wear and corrosion. Pushing past that window trades away the gains. This framing, in which interface stability, rather than reinforcement content, is the true control variable, offers a simple rule for tuning sustainable magnesium composites for service under aggressive sliding contact. The schematic of the tribocorrosion and interface stability mechanism for a well-bonded composite is illustrated in Fig. 12.

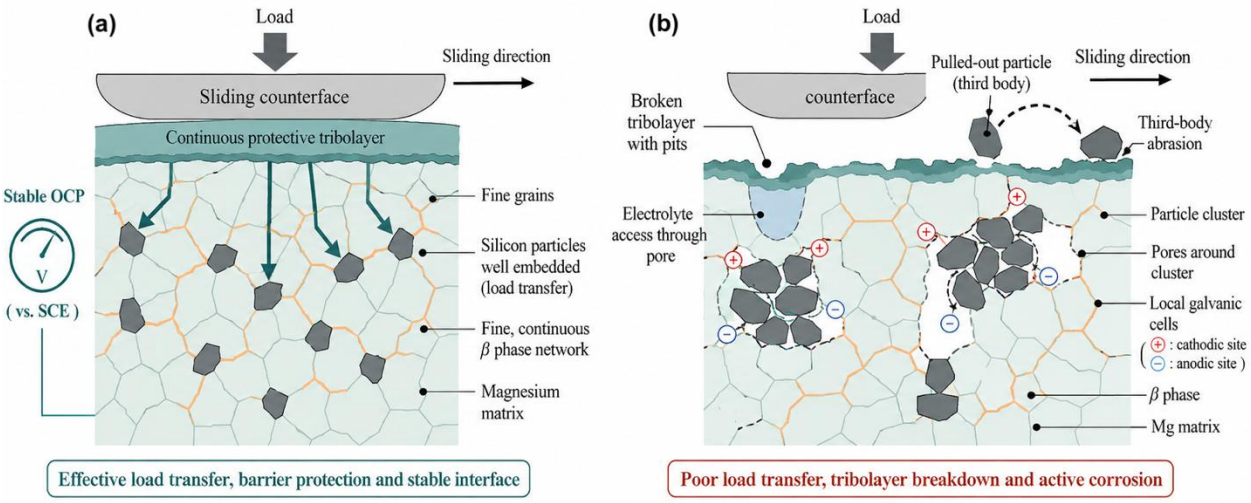


Fig. 12. Schematic of the tribocorrosion and interface stability mechanism for a well-bonded composite (a) and a clustered composite (b).

4. Conclusions

Silicon particles recovered from waste seashells were used to reinforce AZ91 magnesium at 3, 6 and 9 wt% by stir casting, and the combined wear and corrosion behaviour of the composites was studied in 3.5 wt% NaCl. The main findings are as follows.

- The reinforcement refined the α-Mg grains and redistributed the β-Mg17Al12 phase into a finer, more barrier-like network up to 6 wt%. Microhardness increased from about 68 HV in AZ91 to about 102 HV in the 6 wt% composite.

- Static corrosion resistance improved with reinforcement up to 6 wt%. The corrosion current density fell from about 95 to about 34 $\mu A\ cm^{-2}$, and the charge transfer resistance rose from about 480 to about 1350 $\Omega\ cm^2$.
- Dry sliding wear rate and friction dropped with reinforcement, with a wear rate reduction near 58% at 6 wt% as hard particles carried load and supported a protective tribolayer.
- Under tribocorrosion, the 6 wt% composite held a stable open circuit potential during sliding and recovered quickly afterwards.
- Beyond 6 wt%, the particles clustered, porosity increased, and interfaces weakened, thereby reversing the corrosion, wear, and tribocorrosion gains through pull-out, third-body abrasion, and new galvanic sites.
- Interface stability, rather than reinforcement content alone, is the variable that decides whether a waste-derived reinforcement protects AZ91 or accelerates its failure. A design window near 6 wt% gives the best combined durability for the route used here.

Taken together, the study shows that a low-cost, fully waste-derived reinforcement can improve the durability of AZ91 in aggressive sliding contact, and it points to interface control as the route to further gains. Future work should test other electrolytes and loads, quantify the tribolayer chemistry in greater detail, and explore secondary processing, such as friction stir processing, to break up clusters and widen the useful reinforcement window.

Acknowledgement

I would like to thank you Amity School of Engineering and Technology, Greater Noida Campus, Uttar Pradesh, India for providing the research facilities.

Funding

There is no funding received for carrying out this project work.

Data availability

The authors confirm that the data supporting the findings of this study are available within the article. If further required, Data sets generated during the current study could be available from the corresponding author on reasonable request.

Conflict of interest

The authors declare that they have no known competing financial interests or personal relationships that could have appeared to influence the work reported in this paper.

References

1. B.L. Mordike and T. Ebert, Magnesium: Properties, Applications, Potential, Mater. Sci. Eng. A, 2001, 302(1), p 37–45. https://doi.org/10.1016/S0921-5093(00)01351-4
2. D. Prasad, S. Kumar, and R. Kumar, Metal Matrix Composites: Revolutionary Materials for Shaping the Future, Discov. Mater., 2025, 5, 226. https://doi.org/10.1007/s43939-025-00226-6
3. P. Monish, K.L. Hari Krishna, and K. Rajkumar, Manufacturing and Characterisation of Magnesium Composites Reinforced by Nanoparticles: A Review, Mater. Sci. Technol., 2023, 39(12), p 1447–1470. https://doi.org/10.1080/02670836.2023.2194745
4. Corrosion Behaviour of AZ21, AZ501 and AZ91 in Sodium Chloride, Corros. Sci., 1999, 41(2), p 249–273. https://doi.org/10.1016/S0010-938X(98)00078-X
5. M. Jonsson, D. Persson, and D. Thierry, Roles of the β Phase in the Corrosion Process of AZ91D Magnesium Alloy, Corros. Sci., 2006, 48(5), p 1193–1208. https://doi.org/10.1016/j.corsci.2005.05.007
6. V. Pinela et al., Study of the Corrosion Process of AZ91D Magnesium Alloy during the First Hours of Immersion in 3.5 wt.% NaCl Solution, Int. J. Corros., 2018, 8785154. https://doi.org/10.1155/2018/8785154
7. Real-Time in situ Observation of the Corrosion Process of Die-Cast AZ91D Magnesium Alloy in NaCl Solutions under Galvanostatic Polarization, Corros. Sci., 2021, 190, 109642. https://doi.org/10.1016/j.corsci.2021.109642
8. A. Okoani, A. Nand, and M. Ramezani, Tribocorrosion Behaviour of NiTiNOL60 Alloy in an Alkaline Environment, Results Eng., 2023, 19, 101305. https://doi.org/10.1016/j.rineng.2023.101305
9. M. Wood et al., Coatings and Surface Modification of Alloys for Tribo-Corrosion Applications, Coatings, 2024, 14(1), 99. https://doi.org/10.3390/coatings14010099
10. S. Sivakumar and R. Subramanian, Tribocorrosion in Biomaterials and Control Techniques: A Review, Corros. Rev., 2024, 42(1), p 37–56. https://doi.org/10.1515/corrrev-2023-0008
11. A. Review on Wear, Corrosion, and Wear-Corrosion Synergy of High Entropy Alloys, Heliyon, 2024, 10, e25867. https://doi.org/10.1016/j.heliyon.2024.e25867
12. Tribocorrosion Challenges and Surface Engineering Strategies for Magnesium-Based Biodegradable Materials: A Critical Review, Tribol. Int., 2025, 208, 109899. https://doi.org/10.1016/j.triboint.2025.109899
13. A Critical Review on Development of Magnesium-Based Bio-Implants Surface Composite through Friction Stir Processing Route, Crit. Rev. Solid State Mater. Sci., 2025. https://doi.org/10.1080/10408436.2025.2560335
14. Effect of Variation of SiC Reinforcement on Wear Behaviour of AZ91 Alloy Composites, Materials, 2021, 14(4), 949. https://doi.org/10.3390/ma14040949
15. S. Gnanavelbabu et al., Tribo-Corrosive Wear and Mechanical Properties of Nanoparticles Reinforced Mg-AZ91D Composites, Tribol. Int., 2023, 178, 108059. https://doi.org/10.1016/j.triboint.2022.108059
16. A. Gnanavelbabu et al., Tribocorrosion Behaviour of AZ91D Magnesium Alloy Reinforced with Nano Metal Oxides (ZnO, MnO, TiO2), Tribol. Int., 2023. https://doi.org/10.1016/j.triboint.2022.108059

17. M.S. Kumar et al., Enhanced Electrochemical and Tribological Properties of AZ91D Magnesium Alloy via Cold Spraying of Aluminum Alloy, J. Therm. Spray Technol., 2019, 28, p 1985–1998. https://doi.org/10.1007/s11666-019-00915-8

18. A.M. Fathy et al., From Scrap and Waste to Sustainable Uniform and Graded Magnesium Composites: A Science of Valorizing Waste-Derived Feedstocks, Prog. Mater. Sci., 2026, 148, 101374. https://doi.org/10.1016/j.pmatsci.2026.101374

19. I. Dinaharan, S.C. Vettivel, M. Balakrishnan, and E.T. Akinlabi, Influence of Processing Route on Microstructure and Wear Resistance of Fly Ash Reinforced AZ31 Magnesium Matrix Composites, J. Magnes. Alloys, 2019, 7(1), p 155–165. https://doi.org/10.1016/j.jma.2019.01.003

20. Utilizing Bio-Waste as the Reinforcement Particles for the Production of Sustainable Composite Brakes and the Investigation of Its Tribological and Corrosive Performance, Environ. Sci. Pollut. Res., 2022, 29, p 79228–79242. https://doi.org/10.1007/s11356-022-22397-y

21. Gupta, Nikhil, Subodh Barthwal, and Praveen Pachauri. "Sustainable Fabrication and Performance Evaluation of Seashell-derived Silicon Reinforced Magnesium Matrix Composites using Stir Casting." Silicon (2026): 1-17.

22. R. Fernández-Penas et al., A Sustainable One-Pot Method to Transform Seashell Waste Calcium Carbonate to Osteoinductive Hydroxyapatite Micro-Nanoparticles, J. Mater. Chem. B, 2023, 11(32), p 7766–7777. https://doi.org/10.1039/D3TB00856H

23. M.L. Basile et al., Stearate-Coated Biogenic Calcium Carbonate from Waste Seashells: A Sustainable Plastic Filler, ACS Omega, 2024, 9(10), p 11232–11242. https://doi.org/10.1021/acsomega.3c06186

24. Seashell-Derived Calcium for Hydroxyapatite Synthesis: A Review Enhancing Mechanical and Biological Performance through Advanced Methods and Modifications, Polym. Bull., 2025. https://doi.org/10.1007/s00289-025-05973-3

25. Mechanical, Biodegradability and Biocompatibility Behaviour of Seashell and ZrO2 Particulates Reinforced AZ31 Mg Composites, Ceram. Int., 2024, 50(9), p 15234–15246. https://doi.org/10.1016/j.ceramint.2024.02.013

26. D. Kumar et al., A Review of the Design, Processes, and Properties of Mg-Based Composites, Nanotechnol. Rev., 2022, 11(1), p 712–739. https://doi.org/10.1515/ntrev-2022-0043

27. M. Saravana Kumar, S.R. Begum, and M. Vasumathi, Influence of Stir Casting Parameters on Particle Distribution in Metal Matrix Composites Using Stir Casting Process, Mater. Res. Express, 2019, 6(10), 1065d4. https://doi.org/10.1088/2053-1591/ab4045

28. M. Saravana Kumar et al., Experimental Investigation of In-Homogeneity in Particle Distribution during the Processing of Metal Matrix Composites, Silicon, 2021, 13, p 2519–2529. https://doi.org/10.1007/s12633-020-00886-4

29. Development and Characterization of AZ91/AlN Magnesium Matrix Composites via Friction Stir Processing, AIP Adv., 2024, 14(6), 065301. https://doi.org/10.1063/5.0205603

30. Effect of Mg17Al12 Precipitate on Corrosion Behavior and Corrosion Anisotropy in AZ91 Magnesium Alloy, Corros. Sci., 2025, 247, 112782. https://doi.org/10.1016/j.corsci.2025.112782

31. Nano-Enhanced Phase Reinforced Magnesium Matrix Composites: A Review of the Matrix, Reinforcement, Interface Design, Properties and Potential Applications, Materials, 2024, 17(10), 2454. https://doi.org/10.3390/ma17102454

32. Hybrid Magnesium Matrix Composites: A Review of Reinforcement Philosophies, Mechanical and Tribological Characteristics, Rev. Adv. Mater. Sci., 2023, 62(1), 20220294. https://doi.org/10.1515/rams-2022-0294

33. Microstructure and Mechanical Properties of Magnesium Matrix Composites Reinforced by In Situ Reduced Graphene Oxide, Materials, 2023, 16(6), 2495. https://doi.org/10.3390/ma16062495

34. A Comparative Electrochemical Study of AZ31 and AZ91 Magnesium Alloy, Int. J. Corros., 2010, 412129. https://doi.org/10.1155/2010/412129

35. Corrosion Behaviour of High-Pressure Die-Cast AZ91 Alloy in NaCl Solution: Effects of Friction Stir Process at High Rotational Speed, Materials, 2023, 16(20), 6720. https://doi.org/10.3390/ma16206720

36. Enhancing Tribo-Mechanical, Microstructural Morphology, and Corrosion Performance of AZ91D-Magnesium Composites through the Synergistic Reinforcements of Silicon Nitride and Waste Glass Powder, Sci. Rep., 2024, 14, 2804. https://doi.org/10.1038/s41598-024-52804-y

37. M. Sathiskumar and M. Kamaraj, Enhancement in Tribological Characteristics of Friction Stir Processed AZ91D Alloy Composite Reinforced with Molybdenum Disulfide, J. Mater. Eng. Perform., 2024. https://doi.org/10.1007/s11665-024-09943-0

38. N. Tenali, G. Ganesan, and P.R. Babu, An Investigation on the Mechanical and Tribological Properties of an Ultrasonic-Assisted Stir Casting Al-Cu-Mg Matrix-Based Composite Reinforced with Agro Waste Ash Particles, Appl. Eng. Lett., 2024, 9(1), p 46–63. https://doi.org/10.46793/aeletters.2024.9.1.5

39. Wear Prediction of Functionally Graded Composites Using Machine Learning, Materials, 2024, 17(18), 4470. https://doi.org/10.3390/ma17184470

40. Effect of Normal Load on the Tribo-Corrosion Behavior of AZ31B Magnesium Alloy, J. Mater. Eng. Perform., 2025. https://doi.org/10.1007/s11665-025-11556-0

41. Synergistic Enhancement of Mechanical Performance, Corrosion Resistance and Wear Resistance in Magnesium Matrix Composites via FSP-Assisted TiC Reinforcement and WAAM Processing, J. Alloys Compd., 2025, 1035, 181950. https://doi.org/10.1016/j.jallcom.2025.181950

42. Cathodic Secondary Phases Enable Protective Tribocorrosion Layers in Magnesium Alloys, J. Magnes. Alloys, 2026. https://doi.org/10.1016/j.jma.2026.01.017

43. X. Gao et al., Effect of Pulse Current Treatment on Anode Corrosion and Discharge of AZ91 Magnesium Alloy, J. Mater. Eng. Perform., 2024. https://doi.org/10.1007/s11665-024-09799-4

44. New Insights on the Corrosion Mechanism of a Peak-Aged Mg-9Al-1Zn Alloy in a Chloride Environment, J. Alloys Compd., 2020, 838, 155597. https://doi.org/10.1016/j.jallcom.2020.155597

45. Tribocorrosion Behavior of TC18 Titanium Alloy: A Discussion about the Interaction between Galvanic Corrosion and Wear, Tribol. Int., 2024, 191, 109135. https://doi.org/10.1016/j.triboint.2024.109135

46. Sustainable Valorization of Mussel Shell Waste: Processing for Calcium Carbonate Recovery and Hydroxyapatite Production, J. Funct. Biomater., 2025, 17(1), 24. https://doi.org/10.3390/jfb17010024

47. Sustainable Synthesis of Biogenic Hydroxyapatite from Eggshells: Effect of Processing Conditions and Comparative Analysis by FTIR, XRD, and SEM, ACS Omega, 2026, 11(28), p 41432–41444. https://doi.org/10.1021/acsomega.6c02100